

# Spotting Local Environments in Self-Assembled Monolayer-Protected Gold Nanoparticles

Cristian Gabellini, Maria Sologan, Elena Pellizzoni, Domenico Marson, Mario Daka, Paola Franchi, Luca Bignardi, Stefano Franchi, Zbyšek Posel, Alessandro Baraldi, Paolo Pengo, Marco Lucarini,\* Lucia Pasquato,\* and Paola Posocco\*

Cite This: <https://doi.org/10.1021/acsnano.2c08467>

Read Online

ACCESS |

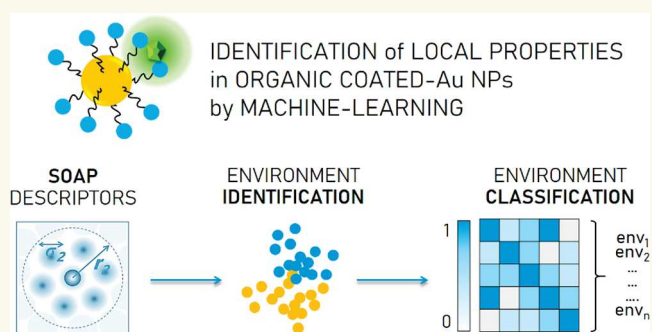
Metrics & More

Article Recommendations

Supporting Information

**ABSTRACT:** Organic–inorganic (O–I) nanomaterials are versatile platforms for an incredible high number of applications, ranging from heterogeneous catalysis to molecular sensing, cell targeting, imaging, and cancer diagnosis and therapy, just to name a few. Much of their potential stems from the unique control of organic environments around inorganic sites within a single O–I nanomaterial, which allows for new properties that were inaccessible using purely organic or inorganic materials. Structural and mechanistic characterization plays a key role in understanding and rationally designing such hybrid nanoconstructs. Here, we introduce a general methodology to identify and classify local (supra)molecular environments in an archetypal class of O–I nanomaterials, i.e., self-assembled monolayer-protected gold nanoparticles (SAM-AuNPs). By using an atomistic machine-learning guided workflow based on the Smooth Overlap of Atomic Positions (SOAP) descriptor, we analyze a collection of chemically different SAM-AuNPs and detect and compare local environments in a way that is agnostic and automated, i.e., with no need of *a priori* information and minimal user intervention. In addition, the computational results coupled with experimental electron spin resonance measurements prove that is possible to have more than one local environment inside SAMs, such as the thickness of the organic shell and solvation primary factors in the determining number and nature of multiple coexisting environments. These indications are extended to complex mixed hydrophilic–hydrophobic SAMs. This work demonstrates that it is possible to spot and compare local molecular environments in SAM-AuNPs exploiting atomistic machine-learning approaches, establishes ground rules to control them, and holds the potential for the rational design of O–I nanomaterials instructed from data.

**KEYWORDS:** mixed monolayers, fluorinated nanoparticles, ESR, multiscale modeling, machine learning, SOAP, nanoconfinement



There is an intense interest in the rational design of organic–inorganic (O–I) hybrid nanomaterials.<sup>1</sup> Installation of organic molecules and specifically thiol-containing ligands on a nanosized gold core is a primary example of such O–I nanoplatfoms. Thanks to reproducible synthetic approaches that enable fine control over size, shape, surface chirality, and dispersion, the easiness to passivate the gold surface by the formation of a self-assembled monolayer (SAM) and to further introduce a variety of functional groups has enabled significant steps forward in the last years, granting access to a plethora of SAM-enabled gold nanoparticles (AuNPs) with functional properties.<sup>2</sup> Indeed, the self-organization of ligands endows SAM-AuNPs with unique molecular recognition and sensing characteristics, which arise

from the collective and cooperative behavior of the organic layer.<sup>3,4</sup> The nanoconfinement imposed to surface-bound molecules dramatically influences their chemical and physical properties, as well as conformation.<sup>5–8</sup> For instance, Kay studied the nanoparticle-confined hydrazone exchange.<sup>9</sup> With the help of molecular dynamics calculations, the work demonstrated that at nanoscale SAM structure and conforma-

Received: August 24, 2022

Accepted: November 29, 2022

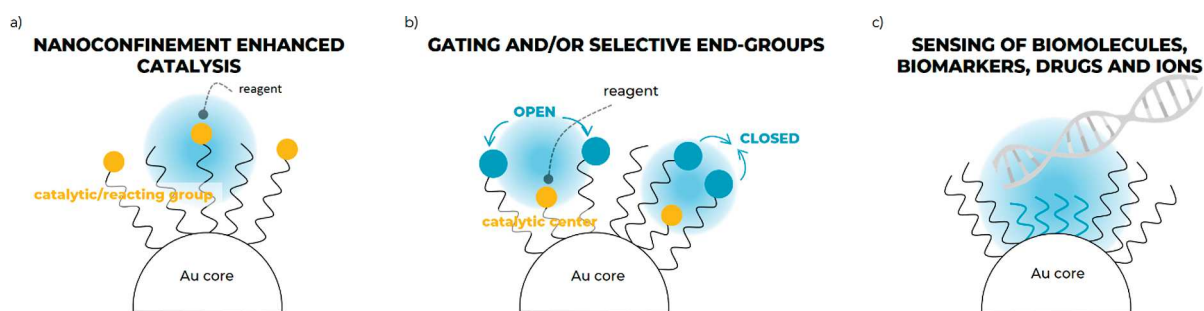


**Figure 1.** Exemplification of the concept of local (supra)molecular environment (highlighted in blue) in SAM-AuNPs and its exploitation. (a) If ligands contain a catalytic group and the surrounding molecules adopt specific cooperative conformation and order, 3D binding sites similar to those in enzymes may arise with enhanced catalytic properties. (b) The end group on the surface switches on/off the access to a catalytic center and grants selective diffusion to the organic layer, causing different local structural features and reagent concentration. (c) Heteroligand monolayers of two immiscible ligands lead to surface anisotropy with implications for surface related biological processes and sensing of biomolecules, biomarkers, and drugs.

51 tional dynamics affects the transport properties and local  
52 concentration of reagent water involved in the exchange, the  
53 accessibility to the reaction sites, and ultimately the overall  
54 reaction kinetics. Grzybowski and collaborators conceived a  
55 mixed SAM-AuNP, in which longer ligands end in “gating  
56 units” able to control both the access and orientation of the  
57 incoming substrates with respect to the catalytic centers  
58 tethered at the end of shorter ligands. Gating and substrate and  
59 site selectivities derived from the molecular details of the on-  
60 particle molecular environment needed to be carefully  
61 designed.<sup>10</sup> Mimicking the catalytic activity of proteins or  
62 their interaction with biological matter exploiting SAM-AuNPs  
63 has also been the object of growing exploration.<sup>11–14</sup> The  
64 integration of bio-orthogonal catalytic systems such as  
65 transition-metal catalysts into nanoparticle scaffolds allowed  
66 the creation of synthetic catalytic nanosystems (nanozymes)  
67 able to replicate the complex behavior of natural enzymes in  
68 biological media.<sup>15,16</sup> Hydrophobicity of surface motifs and  
69 monolayer compaction regulate the kinetic behavior of the  
70 nanozyme, together with temperature or pH.<sup>17,18</sup>

71 The examples cited above point out the beauty and  
72 complexity of surface confined environments in SAMs. They  
73 all rely on the local structure, dynamics, and solvation of the  
74 monolayer at atomic and nanoscale, although to a different  
75 extent. With a broad term, they exploit the features of *local*  
76 (*supra*)molecular environments in SAMs (Figure 1). For  
77 instance (Figure 1b), molecular structure, accessibility, surface  
78 morphology, and local reagent concentration change when the  
79 gate is open or closed. Thus, in this context, we can think of  
80 local (supra)molecular environments as regions of the  
81 monolayer with unique distinct fingerprints. The term  
82 encompasses multiple interconnected effects, such as atom  
83 density, ligand dynamics and conformation, monolayer  
84 structure, and ligand–ligand and ligand–solvent interactions  
85 as well as local solvation or substrate concentration (if any). As  
86 such, they are hard to anticipate and only few of them can be  
87 directly assessed with experiments by using techniques such as  
88 NMR,<sup>19–21</sup> SANS,<sup>22</sup> MALDI-TOF,<sup>23</sup> and ESR;<sup>24,25</sup> yet, these  
89 techniques suffer of some limitations, as the monolayer needs  
90 to be designed *ad hoc* for the specific technique.

91 Thus, we wondered if a general way to identify specific local  
92 settings in SAMs could exist. Molecular dynamics (MD) and  
93 coarse-grained simulations have been instrumental in retrieving  
94 information difficult to infer from experiments and in  
95 explaining the behavior of SAM-AuNPs at molecular and

nanoscale with good reliability.<sup>26–29</sup> Over recent years, the 96  
increasingly large amounts of data produced by these 97  
calculations have also been used by algorithms to extrapolate 98  
molecular patterns and predict (meta)stable configurations or 99  
structural motifs in complex matter.<sup>30–32</sup> 100

Here, in a proof-of-concept study, we introduce a two-step 101  
computational workflow able to detect first and then compare 102  
local (supra)molecular environments in SAM-AuNPs with no 103  
need of predefined information and minimal user intervention. 104  
It combines atomistic all-atom MD (AA-MD) calculations and 105  
the Smooth Overlap of Atomic Positions (SOAP) descriptors 106  
for machine-learning guided analysis. The retrieved local 107  
environments are then described and rationalized by MD 108  
calculations and supported by experiments of electron spin 109  
resonance (ESR), a spectroscopic technique highly sensitive to 110  
polarity changes in the local background perceived by a radical 111  
probe,<sup>25</sup> that are carried out at different temperatures. 112

A set of AuNPs (roughly 4.0 nm in size), which support 113  
homo- and hetero (mixed)-SAMs composed of thiolates 114  
ending in positive (ligands 1 and 2) or negative (ligands 3 115  
and 4) or zwitterionic (ligand 5) charged end groups and short 116  
fluorinated ligands (ligand 6) (Figure 2), is tested. We sought 117  
to augment the complexity of the monolayer by including 118  
fluorine containing mixed SAMs, which are particularly 119  
relevant for driving surface phase separation,<sup>21,26</sup> controlling 120  
hydrophobicity or superhydrophobicity of surfaces,<sup>33</sup> or 121  
tuning the molecule–NP interaction.<sup>34</sup> 122

Hereafter, we adopt the following notation: NP1 indicates a 123  
SAM of ligand 1 on AuNP while NP1/6, a SAM of ligand 1 124  
and 6 on AuNP. 125

The paper is organized as follows: first, NP structure and 126  
properties from AA-MD simulations in solvent (water) are 127  
discussed; second, the computational approach for the 128  
identification and comparison of local motifs in different 129  
SAMs is illustrated and the outcomes considered; third, the 130  
results are interpreted in light of ESR investigation. 131

Overall, this work not only demonstrates that it is possible to 132  
spot local (supra)molecular environments in SAM-AuNPs by 133  
exploiting atomistic data-driven approaches but also is a step 134  
toward the design of functional nanoparticles with a program- 135  
mable response. 136

## RESULTS AND DISCUSSION 137

**MD-Derived SAM-AuNP Characterization.** The specific 138  
structure of the monolayer is imparted by the self-organization 139

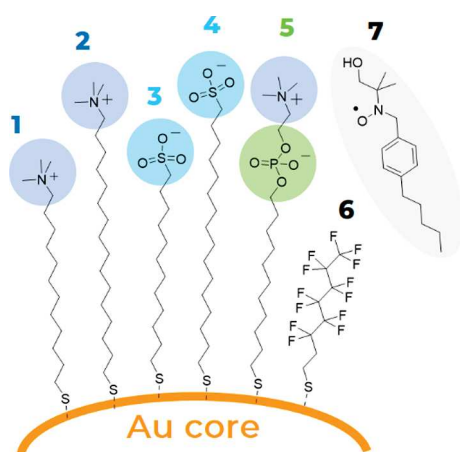


**Figure 2.** Structure of the thiolates 1–6 for the AuNP coating. Radical probe 7 for ESR investigation. Ligand 6 is used in mixed monolayers with 1–5. Thiolates differ in nature and charge of the terminal group (1 and 2, a positively charged quaternary ammonium ion; 3 and 4, a negatively charged sulfonate ion; 5, a zwitterionic group, composed by a trimethylammonium and a phosphate group) as well as in length of the alkyl chain ( $C_{12}$  in 1, 3, 5;  $C_{16}$  in 2, 4).

140 of the individual thiolates on the surface of the gold core. We  
141 have very recently demonstrated by calculations<sup>28</sup> that the  
142 surface morphology depends on size and hydrogen bonding  
143 capability of the ligand end group, while other features, such as  
144 the alkyl chain length or the core size, affect the final ligand  
145 organization less. In particular, a large space-filling group like  
146 trimethylammonium or zwitterionic ones give rise to spatially  
147 uniform arrangements due to the steric hindrance of bulky  
148 terminal moieties; small end groups like sulfonate allow

association of the chains in bundles, which instead leads to  
149 anisotropic shells (Figures 3 and S1). The combination of  
150 more than one kind of ligand in the shell has long been used in  
151 the nanoparticle community to tune nanoparticle solubility,  
152 wettability, interfacial properties, hydrophobic interactions for  
153 self-assembling nanoparticles, respond to the surrounding  
154 (bio)environment, and induce nanoscale surface morpholo-  
155 gies.<sup>4,35–39</sup>

156 Indeed, when a mixture of dissimilar and/or immiscible  
157 molecules are employed to coat AuNPs, nanoscale domains  
158 may spontaneously form in the shell via ligand surface  
159 rearrangement.<sup>40</sup> Fluorinated ligands are known to be highly  
160 lipophobic, and we have already tested their ability to trigger  
161 phase separation in 3D SAMs when used in combination with  
162 hydrogenated thiolates even at low molar fraction.<sup>21,26</sup> Here,  
163 we have carried out auxiliary mesoscale simulations (to cope  
164 with the slow evolution of the phase separation at the  
165 nanoscale)<sup>41</sup> coupled with AA-MD calculations in water to  
166 predict the pattern of organic shells containing fluorinated  
167 thiolates, namely, ligand 6. For details on molecular models  
168 and simulations, see the [Experimental Section](#) and [Supporting](#)  
169 [Information \(SI\) Section S3](#). Gold size, ligand density, and  
170 monolayer composition have been assigned to closely match  
171 those obtained experimentally (see [SI Section S2](#)).  
172

173 The calculations confirm that, irrespective to the chemical  
174 nature and the chain length of the primary ligand (i.e., 1–5),  
175 ligands 6 separate in small domains (Figures 3 and S1). For  
176 AuNPs bearing sulfonates and zwitterionic moieties as surface  
177 groups (namely, NP3/6, NP4/6, and NP5/6) these domains  
178 appear as elongated patches with an average width of 1.6–1.9  
179 nm and length of 2.7–3.6 nm. Stripe-like patterns are indeed  
180 present on NP1/6 and NP2/6, where the bulkier headgroups  
181 favor the formation of domain interfaces more (Figure S2).<sup>42</sup>

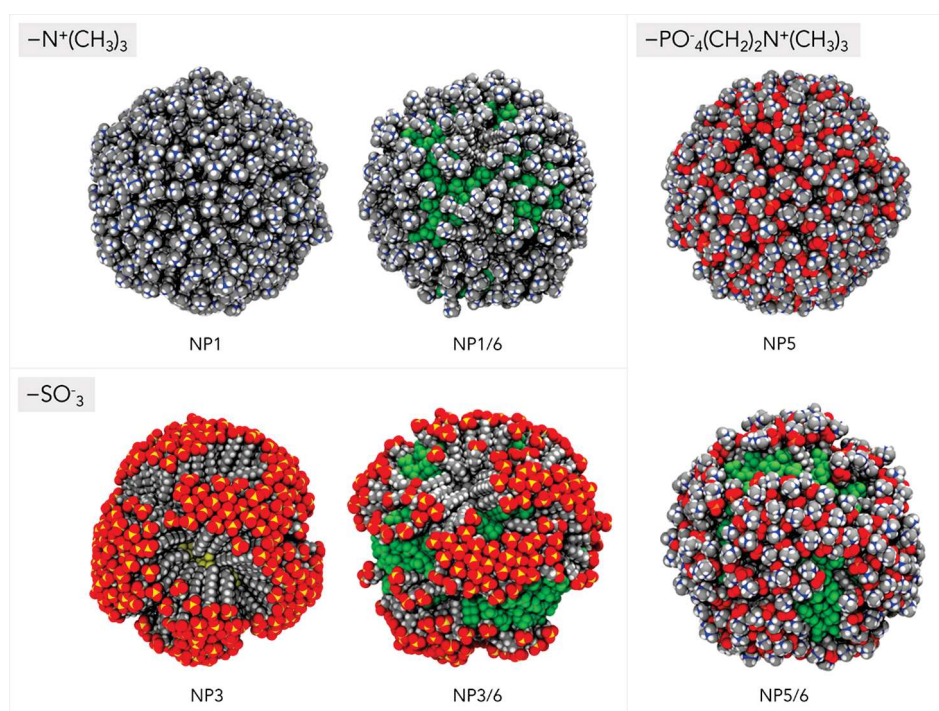


**Figure 3.** Representative molecular structures of homoligand NP1, NP3, and NP5 AuNP and its heteroligand NP1/6, NP3/6, and NP5/6 counterpart from molecular dynamics simulations in explicit solvent (water). For clarity, water and counterions are not shown. Color representation of atoms: C, gray; O, red; S, yellow; P, orange; N, blue; F, green; H, white.



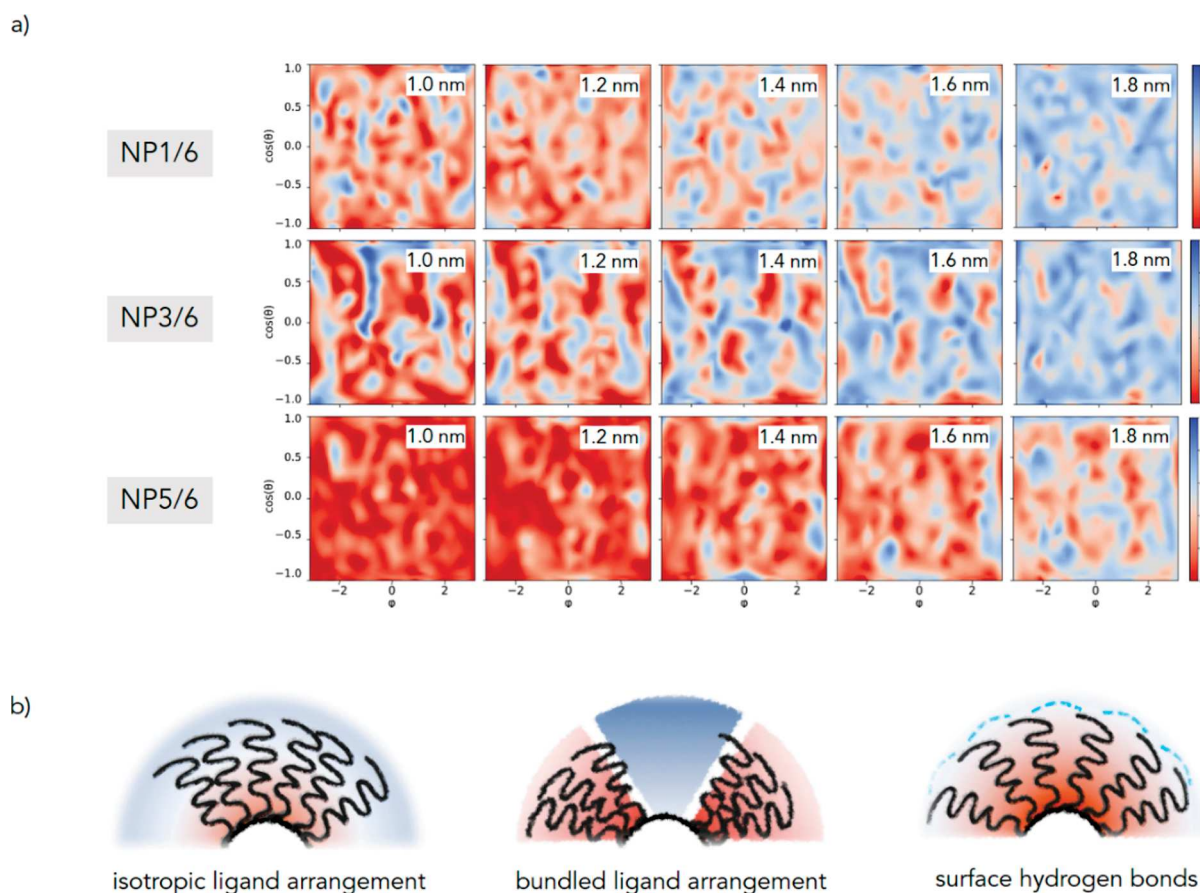


**Figure 4.** (a) Normalized water distribution at increasing distance from the gold surface for NP1/6, NP3/6, and NP5/6. The graphs plot the distribution of the atom (oxygen of water or carbon of thiulates) closest to gold surface (centered on the gold core and placed at increasing distances from its surface) shown as a two-dimensional projection of the sphere surface ( $x$ -axis, the azimuthal angle  $\varphi$ ;  $y$ -axis, the cosine of the polar angle  $\theta$ ). A value of 1 indicates that an oxygen atom of a water molecule is always the closest; if it is equal to 0, it indicates that a carbon/fluorine atom of a chain is always the closest. Simplifying, red to salmon areas represent poorly hydrated zones, while blue areas stand for highly hydrated parts of the monolayer (at a certain distance from the gold surface). At distances lower than those considered, the microenvironment is almost hydrophobic, while at higher distances, it is fully hydrated and no major difference between the monolayers could then be detected. Maps for NP2/6 and NP4/6 can be found in the SI (Figures S5 and S6). (b) Examples of possible different hydration states within SAMs.

182 The phase separation does not alter the propensity of the  
 183 most abundant ligand to associate in bundles. Thus, NP3/6  
 184 and NP4/6 have a spatially heterogeneous ligand distribution  
 185 as is also observed for their homoligand counterpart NP3 and  
 186 NP4 (Figures 3 and S1). The clustering (or bundling) of  
 187 ligands can be quantified by means of Voronoi diagrams, which  
 188 allow local density estimation through nearest neighbor  
 189 analysis<sup>43</sup> (Figures S3 and S4). In both monolayers, the  
 190 presence of high-density regions where the chains form  
 191 bundles is evident and these roughly correspond in number  
 192 to those identified using a different clustering algorithm (e.g.,  
 193 HBDSCAN, see SI Table S1), supporting the presence of time-  
 194 persistent aggregation of ligands. Regular and more uniform  
 195 patterns instead characterize the Voronoi diagram of NP1,  
 196 NP3, and NP5 and their heteroligand partners NP1/6, NP3/  
 197 6, and NP5/6 (Figures S3 and S4) consistently with an  
 198 isotropic distribution of the ligands around the gold core. The  
 199 results also highlight that long ligands (i.e., HS-C<sub>16</sub>-FG) on  
 200 nanoparticled induce more heterogeneous ligand distributions,  
 201 which appeared clearly from the visual inspection of the  
 202 diagrams (e.g., compare Figures S3a and S4a or Figures S3c  
 203 and S4c). Yet, a simple measure is provided by the area  
 204 dispersion index (ADI), which describes the spread of the

tessellation cell areas (see SI Section S3.3 for how ADI is  
 205 calculated) (Table S1). For NP1, ADI is equal to 2.24 and  
 206 increases to 2.52 for NP2, indicating a broader distribution of  
 207 the area available for each ligand; the increased local  
 208 heterogeneity in long chains has also been seen by others,<sup>44</sup>  
 209 and it is promoted by higher interchain van der Waals  
 210 interactions and higher free chain volume due to the increased  
 211 radiality. For anisotropic shells like NP3 and NP4, this  
 212 phenomenon is less evident from ADI analysis (ADI is equal to  
 213 2.96 and 3.12, respectively) but still detectable in the diagrams.  
 214 Adding a second ligand in the monolayer does not affect the  
 215 overall monolayer structure yet impacts the ligand local order.  
 216 Indeed, for almost all the heteroligand monolayers, the ADI  
 217 decreases compared to the homoligand AuNP, thus indicating  
 218 a more uniform distribution of the space available for each  
 219 chain, likely because of the bulky fluorinated alkyl thiulates.  
 220 Further structural analysis of the monolayer is available in  
 221 Tables S1 and S2. 222

Revealing monolayer structure and molecular order is the  
 223 first necessary step to gather information about nanoparticle  
 224 hydration and solvation-related properties.<sup>45</sup> Previous exper-  
 225 imental and computational efforts<sup>46–48</sup> have highlighted that  
 226 ligand ordering is more correlated than other conventionally  
 227

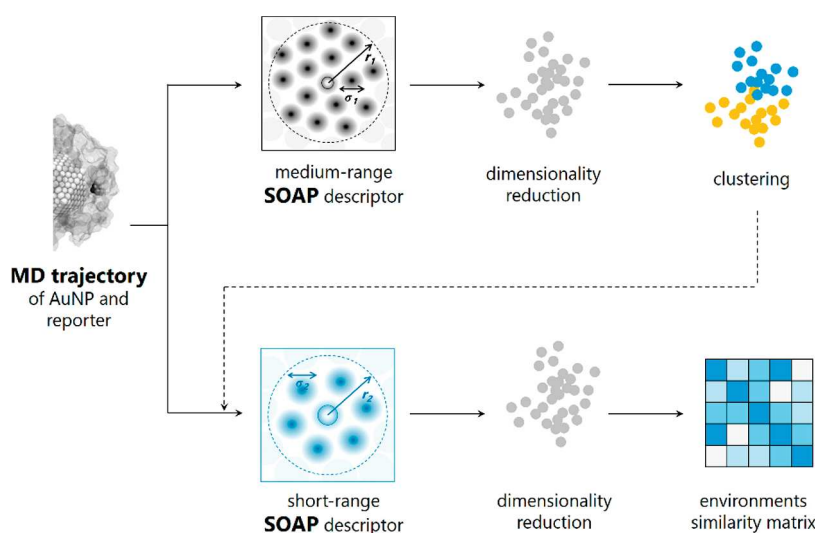


Figure 5. Conceptual diagram of the workflow used for the detection and comparison of local molecular environments within self-assembled monolayers (SAMs) using the Smooth Overlap of Atomic Positions (SOAP)-based structural analysis. Molecular dynamics calculations of the SAM-AuNP and reporter 7 are conducted in explicit solvent. The SOAP descriptor vector is constructed taking the reporter atoms (here the nitrogen atom) as the center of the structural environment up to a given cutoff radius  $r_1$  (medium-range description) and employed for the identification of molecular fingerprints assigned by an unsupervised clustering algorithm (step 1). The short-range SOAP descriptor is built considering only solvent molecules up to a range of  $r_2$  ( $< r_1$ ), and a linear kernel between SOAP vectors is used to measure the similarity between the environments (step 2) and interpreted by correlating the location of the data with the MD evidence. For more details on each step, see Figure S8 and Section S3 in the SI.

228 considered chemical properties (such as the solvent-accessible  
229 surface area (SASA)) with the interfacial hydrophobicity of  
230 SAMs. Most of the studies have been conducted on planar  
231 SAMs and, when extended to curved surfaces, were focused  
232 only on the description of the SAM–water interface. Here, we  
233 expand the investigation of nanoparticle hydration to the  
234 whole interior of the monolayer and we also consider the  
235 consequences of having mixtures of ligands bearing different  
236 hydrophobicities. To do that, we relate the normalized water  
237 content and the spatial distribution of water molecules within  
238 the monolayer at increasing distances from the core and we  
239 project it onto bidimensional planes. This provides an  
240 immediate view of the average degree of solvation of the  
241 monolayer and the topological distribution of the solvent  
242 within the monolayer (Figure 4).

243 When one observes the water density maps reported in  
244 Figure 4, it appears that isotropic monolayers allow a uniform  
245 diffusion of the solvent within the organic layer; the water  
246 content decreases progressively when moving toward the  
247 nanoparticle center, and there is a concentration gradient with  
248 respect to bulk solution (Figure 4b). On the contrary, the  
249 presence of bundles generates alternation of highly hydrated  
250 zones between the bundles (at a level comparable to that of  
251 bulk solvent) and dehydrated areas, where solvent penetration  
252 is hindered by the strong self-association among bundled alkyl  
253 chains.

254 An additional element affecting the hydration is the  
255 existence of the extended ligand/water hydrogen bond  
256 network on the nanoparticle surface, which reduces the  
257 internal diffusion of the solvent and makes zwitterionic  
258 nanoparticles less hydrated than other isotropic systems, like  
259 for example NP1.

260 Fluorine-rich ligands 6 are considerably shorter than all the  
261 other thiolates; thus, when they segregate in domains, they  
262 enable the local diffusion of the solvent closer to gold, resulting  
263 in a higher content of water with respect to homoligand

AuNPs at the same distance from the gold surface (see also  
Figures S5–S7).

#### Automated Detection of Local (Supra)Molecular Environments in SAM.

The calculations just described are the entry points of an automated workflow able to identify first and then compare local (supra)molecular environments within any SAMs. It is based on the combination of AA-MD calculations of SAM-AuNP carried out in explicit solvent, an agnostic machine-learning structural analysis employing the SOAP<sup>49</sup> formalism to describe the 3D atomic environment that surrounds a reporter molecule (here, the radical probe 7; see Figure 2) interacting with the monolayer, and an unsupervised probability-based method for clustering the data (Figure 5). In the SOAP framework, the local atomic environment of an atom (defined as a SOAP center) is represented by the sum of element-specific smooth Gaussian densities centered on the positions of neighborhood atoms within a spatial cutoff, and it is associated with a vector, commonly known as “SOAP power spectrum” or “SOAP fingerprint” (see SI Section S3 for the SOAP formal derivation). SOAP vectors provide a high-dimensional, agnostic representation of molecular environments. SOAP descriptors have been successfully applied in exploring the conformational landscape of single molecules,<sup>50</sup> recognizing local structural motifs<sup>51</sup> and describing formation/dynamics of soft supramolecular fibers,<sup>52</sup> returning a rich structural/dynamical characterization of complex molecular systems. Such an analysis in our systems allows us to unveil different states of the molecular reporter 7 based on differences in the local environment (microenvironment) that surrounds it during the AA-MD simulation time, accounting for overall atomic composition, molecular conformation, local order, persistency in the interactions, and degree of solvation.

The workflow consists of two main steps both starting from an (equilibrated) AA-MD trajectory of a specific SAM-AuNP/7 complex. The first one is the classification of the local states

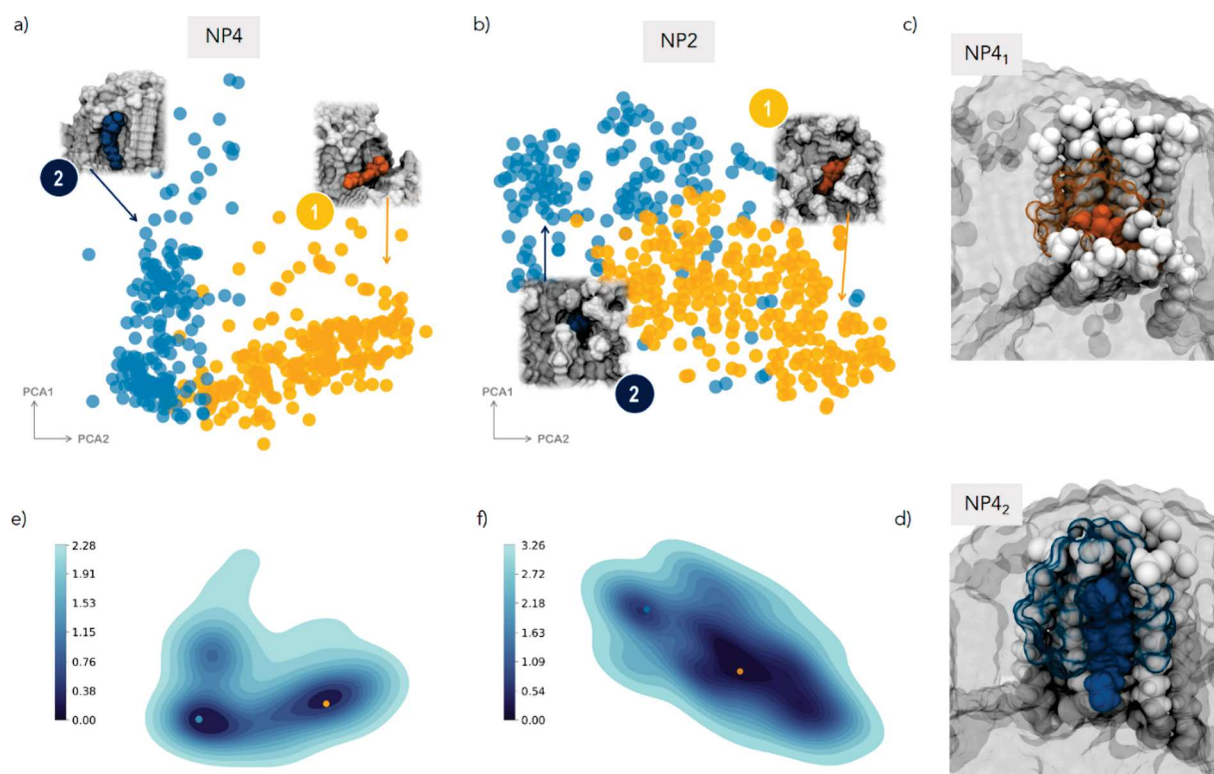


**Figure 6.** First two principal components (PCA1 and PCA2) obtained from dimensionality reduction of the medium-range SOAP feature space of the probe 7 in thicker homoligand NP4 (a) and NP2 (b). Dots are colored according to the clusterization obtained by the GMM analysis. For each cluster, the inset shows the molecular environment centered on the probe 7, extracted from the corresponding MD frames. Color legend: probe, same color of the cluster; ligands 4 and 2 in gray; solvent not shown for clarity. (c, d) Example of the molecular view of the local environments NP4<sub>1</sub> and NP4<sub>2</sub> including all atoms within the cutoff  $r_1$ . The reporter is colored according to the cluster assigned as a sphere; water is shown in the same color of the probe but as a transparent surface, and the ligands belonging to the environment are highlighted as white spheres. The remaining ligands are left as a background gray surface. (e, f) Free energy surface (FES) (kcal/mol) calculated from the state's probability distribution in (a) and (b), respectively. Dots identify the minima on the FES and are colored based on the microstate (cluster) they refer to.

300 of the probe (step 1) (Figure 5 and flowchart in Figure S8). To  
 301 identify the relevant microenvironments visited by 7, the  
 302 SOAP descriptors are calculated to be centered on the nitrogen  
 303 atom of the probe. The SOAP data set includes all atoms  
 304 within a cutoff radius  $r_1$  (9 Å), which is taken as a compromise  
 305 between the ability to capture relevant local structural  
 306 correlations and necessity to minimize the computational  
 307 requirements for SOAP manipulation and storage (see SI  
 308 Section S3, Figure S23). We refer to that as “medium-range  
 309 SOAP vector”.

310 Linear principal component analysis (PCA) is then applied  
 311 to reduce the high dimensionality of the SOAP features space  
 312 (14354 dimensional on average) without losing important  
 313 features. ~94% of the total variance (e.g., global information)  
 314 is retained keeping the first 10 principal components (Figure  
 315 S24). Then, a probabilistic model based on Gaussian mixtures  
 316 (GMMs) is exploited as an unsupervised clustering scheme.  
 317 This allows one to partition and classify all the environments  
 318 perceived by the probe into groups (i.e., clusters) and  
 319 distinguish them without any prior information on the number  
 320 of clusters (for a description of the clustering algorithm, see SI  
 321 Section S3). The outcomes of PCA are visualized by projecting  
 322 the 10 PCs in 2D onto the first two principal components,  
 323 PCA1 and PCA2, to provide simple and intuitive maps.

324 Through the SOAP-GMM analysis, two distinct states (i.e.,  
 325 microenvironments) are identified for NP4 (Figure 6a): the  
 326 probe 7 lays at the ligand bundle–water interface close to the

gold core (1, orange) or parallel to ligand chain (2, blue). 327  
 From now on, each local environment is reported in subscript: 328  
 for example, NP4<sub>1</sub> indicates the local environment (1) in NP4. 329

As an example, Figure 6c,d shows a molecular view of the 330  
 ligands and water molecules forming the local environments 331  
 NP4<sub>1</sub> and NP4<sub>2</sub>. From the MD trajectory, we also calculate the 332  
 free energy surface (FES) of the reporter 7 in the system as the 333  
 probability distribution of states in the PCA reduced SOAP 334  
 feature space (P) by using the standard statistical relation FES 335  
 $= -K_b T \log(P)$  and find that the states correspond to two local 336  
 minima equally visited by 7 (Figure 6e). The classification is 337  
 fully consistent with our previous findings,<sup>28</sup> where two distinct 338  
 positions of 7 were also identified by classical analysis of the 339  
 MD trajectory in NP4, one more deeper in the organic layer 340  
 and one more exposed to the exterior. 341

Two structural states are also detected in NP2 (Figure 6b), 342  
 meaning that thicker monolayers are able to host a small 343  
 molecule in structurally distinguishable *loci*. Yet, inspection of 344  
 the clusterization maps suggests that the difference between 345  
 the two states is sharper in bundled shells. In fact, in NP4, the 346  
 clusters are well distinct and clearly separated; in NP2, the 347  
 transition is smoother, although measurable by SOAP-GMM. 348  
 We attribute this to the diverse ligand arrangement in NP2 and 349  
 NP4. Chain packing allows accommodation of a small 350  
 molecule like 7 by simple binding at the ligand bundle 351  
 interface at increasing depth from the outer surface, and the 352  
 search of an optimal interaction position for the probe is 353



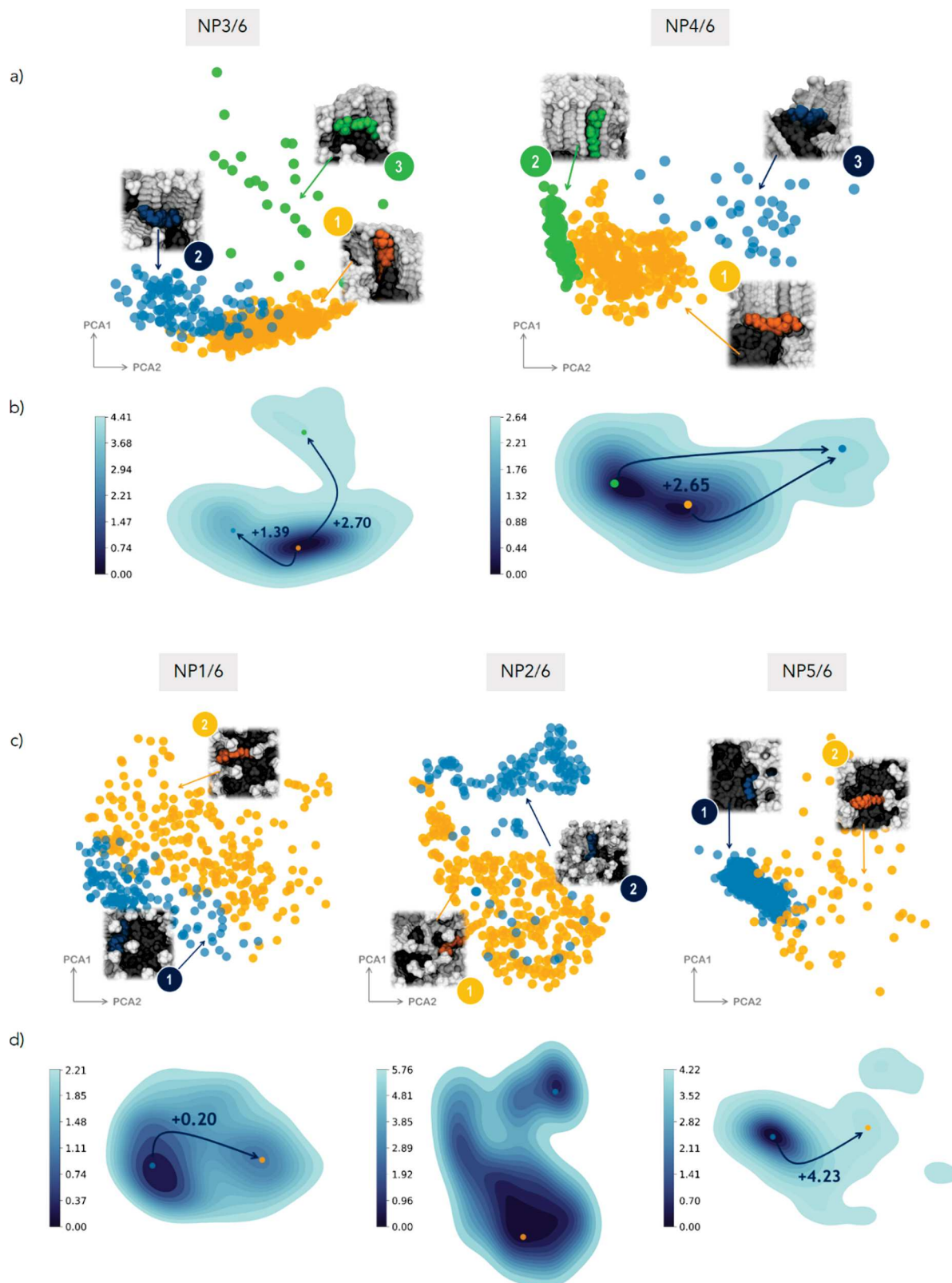


**Figure 7.** First two principal components (PCA1 and PCA2) obtained from dimensionality reduction of the medium-range SOAP feature space of the probe 7 in heteroligand bundled NP3/6 and NP4/6 (a) and isotropic NP1/6, NP2/6, and NP5/6 (c) monolayers. Dots are colored according to the clusterization obtained by the GMM analysis. For each cluster, the inset shows the molecular environment centered on the probe 7, as extracted from the corresponding MD frames. Color legend: probe, same color of the cluster; ligands 1–5 colored in gray; ligand 6 colored in dark gray; solvent not shown for clarity. (b) Free energy surface (FES) (kcal/mol) calculated from the state's probability distribution for NP3/6 and NP4/6 (b) and NP1/6, NP2/6, and NP5/6 (d). Dots identified the minima on the FES and are colored based on the microstate (cluster) they refer to. The arrows indicate the transition probabilities between the states from the minimum.

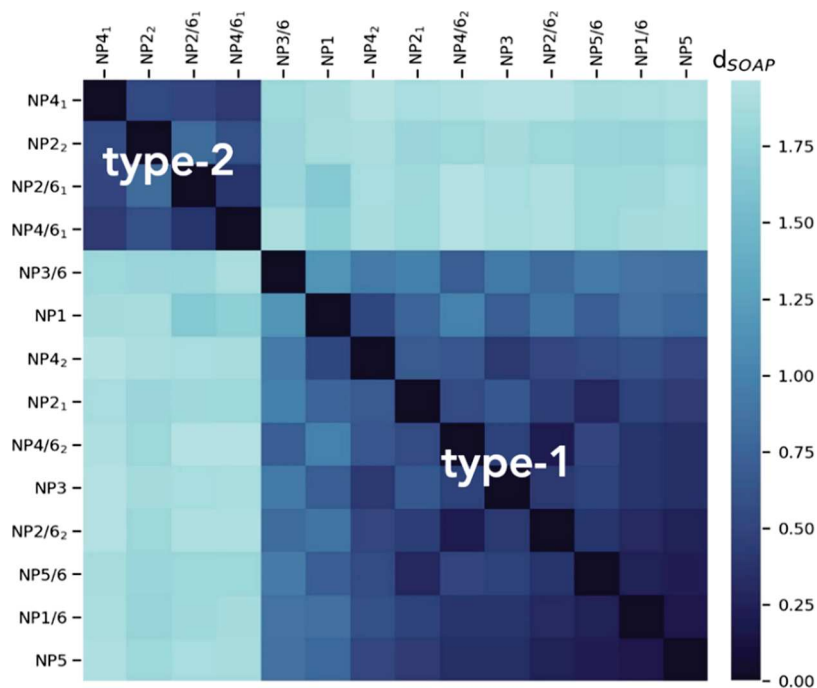


**Figure 8.** Similarity matrix for all local (most visited) environments generated by calculating the pairwise SOAP kernels  $K_{\text{SOAP}}$  between all the reduced short-range SOAP feature vectors. Dark blue color indicates high similarity between the environments.

354 facilitated by the freedom to explore the conformational space  
355 at that interface; this would lead to well-defined binding sites  
356 for NP4.

357 On the other hand, in isotropic monolayers as NP2, the  
358 accommodation of a guest requires diffusion within the ligands,  
359 hampering the access to the whole depth of the monolayer and  
360 thus leveling out differences between interaction positions.

361 When the SOAP-GMM classification is applied to nano-  
362 particles having a shorter hydrophobic portion like NP1 and  
363 NP3, one single microenvironment is identified for 7 (see  
364 Figure S9). Although NP5 could be assimilated to NP1 and  
365 NP3, the classification returns a different picture (Figure S9);  
366 in fact, it unveils the presence of two clusters, namely, two  
367 states explored by the probe. Nevertheless, the FES indicates  
368 that one of them is much more visited than the other and sets  
369 itself as a local minimum. The more complex behavior of the  
370 zwitterionic NP5 reflects the uniqueness of this monolayer in  
371 agreement with the evidence from the AA-MD calculations.

372 Mixed shells containing hydrophobic patches enrich the  
373 probe state space compared to their respective homoligand  
374 nanoparticles. There is a marked difference between bundled  
375 and isotropic monolayers (Figure 7).

376 NP3/6 and NP4/6, which have ligand clusters, show three  
377 (metastable) local environments for the probe: the first on the  
378 fluorinated chains (NP3/6<sub>3</sub> and NP4/6<sub>3</sub>) being the least  
379 visited, the second down at the interface between alkyl and  
380 fluorinated domains (NP3/6<sub>2</sub> and NP4/6<sub>1</sub>), and the third with  
381 the probe parallel to the bundles (NP3/6<sub>1</sub> and NP4/6<sub>2</sub>). The  
382 three states are distinct and clearly separated in the SOAP  
383 feature space. On the contrary, in isotropic monolayers like  
384 NP1/6 and NP2/6, there are only two states possible, which  
385 are not so well divided in the SOAP space as in NP3/6 and  
386 NP4/6, thus highlighting the importance of the monolayer  
387 arrangement in shaping local environments. An exception is  
388 the zwitterionic NP5/6 for which the interfacial NP5/6<sub>1</sub> is  
389 highly favorable and well distinguished from NP5/6<sub>2</sub>. From

the FES inspection, still in heteroligand monolayers, two states  
390 are the most probable for C<sub>16</sub> long chains (i.e., NP2/6 and  
391 NP4/6), and these reduce to one for shorter ligands (NP1/6,  
392 NP3/6, and NP5/6).  
393

**Comparison of Local Environments in Different**  
394 **SAMs.** Once the most probable interaction site(s) is identified  
395 for each system, we want to *compare* them (step 2 of the  
396 workflow, Figure 5). This means assessing how much those  
397 local environments are similar; they belong to either the same  
398 monolayer or to different nanoparticles. To ensure that the  
399 SOAP analysis is meaningful and fully comparable across  
400 different systems, one needs to choose a representation of the  
401 structural space that takes into account common features  
402 between systems. For that reason, we select the (roughly) first  
403 hydration layer of the reporter 7. This choice also allows us to  
404 limit the computational costs, since now all the systems have to  
405 be analyzed together. The nitrogen atom of the probe 7 is still  
406 assigned as the SOAP center, and the cutoff radius  $r_2$  is now set  
407 to 4.5 Å (Figure S23), including only solvent molecules. We  
408 refer to that as “short-range SOAP”. Accordingly, taking the  
409 MD snapshots where the probe is in the most favorable  
410 state(s) based on the assignment of the medium-range SOAP-  
411 GMM clusterization, we construct the corresponding short-  
412 range SOAP fingerprint for each molecular environment and  
413 each nanoparticle. Then, we perform a dimensionality  
414 reduction via linear PCA to obtain a low-dimensional  
415 representation and consider only the first 10 components  
416 (Figure S24).  
417

Measuring structural similarity requires the definition of a  
418 metric that is capable of identifying identical molecular  
419 fingerprints. There are different ways of combining atom-  
420 centered representations to obtain a structure-level compar-  
421 ison;<sup>53</sup> in the SOAP space, one natural choice is to define a  
422 linear kernel of the density representation in the form of the  
423 dot product of the SOAP power spectra of the two molecular  
424 environments  $K(i,j)_{\text{SOAP}}$  (see SI Section S3). SOAP-based  
425



426 structural similarity kernels can be interpreted as a measure of  
 427 how much two (smoothed) atomic distributions ( $i,j$ ) are  
 428 superimposed on each other (i.e., how much similar the local  
 429 environments are in the SOAP space). The data are displayed  
 430 in the form of a similarity matrix by converting the similarity  
 431 value  $K(i,j)_{\text{SOAP}}$  to an Euclidean distance metric  $d_{\text{SOAP}}$ , ranging  
 432 from 0 to 2 (Figure 8).

433 The color level is proportional to the value of the similarity  
 434 between environments: dark blue corresponds to the highest  
 435 value of similarity computed and light blue indicates larger  
 436 SOAP distances and an increased structural difference between  
 437 the environments. From Figure 8, it appears evident that there  
 438 are two distinct classes of environments according to the  
 439 similarity metric: the first one (type-1) is that corresponding to  
 440 the lower right quadrant of the matrix and the second (type-2),  
 441 to the upper left quadrant.

442 It is worth noting that the classes are not equally populated.  
 443 Type-2 includes only a few molecular environments, of which  
 444 all exist in thick monolayers (namely, NP2- and NP4-type  
 445 nanoparticles), while the type-1 class is broader and comprises  
 446 environments from long ( $-S-C_{16}-FG$ ) to short ( $-S-C_{12}-$   
 447  $FG$ ) chain shells. This interesting piece of evidence suggests  
 448 that thick ( $\geq C_{16}$ ) monolayers have the ability to form local  
 449 environments with structural features well distinguishable from  
 450 those existing in thin monolayers. In addition, the results show  
 451 that it is possible to capture and discriminate multiple  
 452 environments applying a pure data-driven evaluation without  
 453 *a priori* assumptions.

454 To gain more insights and in an attempt to rationalize these  
 455 outcomes, we then link each state to the corresponding  
 456 molecular structure retrieved from the MD snapshots as  
 457 assigned by the medium-range SOAP-GMM to that environ-  
 458 ment; in this way, we find out that nanoparticles with a single  
 459 interaction site (namely,  $-S-C_{12}-FG$ ) are classified as type-1;  
 460 in systems with two main interaction sites, one is of type-1 and  
 461 the other is of type-2. Type-2 sites correspond to local  
 462 environments where the probe is placed closer to the gold core  
 463 and the overall hydration is limited (as an example, see Figure  
 464 6c for NP4<sub>1</sub> or Figure 7a for NP4/6<sub>1</sub>). We assess that by  
 465 simply calculating the radial distribution function (RDF) of the  
 466 nitrogen atom of the reporter (i.e., the probability distribution  
 467 as a function of distance from the metal center) from the  
 468 corresponding MD frames and matching the peak of the RDF  
 469 with the solvation map to that distance. Type-1 environments  
 470 instead share a higher solvation, and the probe is more exposed  
 471 to the external environment (as an example, see Figure 6d for  
 472 NP4<sub>2</sub> or Figure 7a for NP4/6<sub>2</sub>). The chemistry of the thiolates  
 473 end group has no major influence on the features of the  
 474 interaction site, which is not completely surprising since the  
 475 probe is mainly interacting with the alkyl part of the ligands  
 476 (Figures 6, 7, and S9).

477 **ESR Analysis of SAM-AuNPs.** Experimentally, monolayer  
 478 features can be investigated by molecular probes, which are  
 479 able both to enter inside the monolayer and to possess spectral  
 480 features that depend on the molecular environment of the  
 481 surroundings. Functionalized benzyl *tert*-butyl nitroxides  
 482 (BTBN) possess such characteristics and have been largely  
 483 employed to characterized different types of water-soluble  
 484 SAM-protected AuNPs.<sup>54–57</sup> In the present study, probe 7  
 485 containing a pentyl chain at the *para* position of the aromatic  
 486 ring and a hydroxymethyl group in place of the methyl in the  
 487 *tert*-butyl substituent is employed for ESR investigation. This  
 488 hydrophobic probe has been chosen because of its good

489 affinity for the nanoparticle organic monolayer when dissolved  
 490 in water. Experimental values of hyperfine splitting constants  
 491 (hfsc's) of heteroligand nanoparticles are collected in Table 1

**Table 1. Spectroscopic Parameters for Radical Probe 7 at Different Temperatures (Black at 300 K and Light Blue at 340 K)**

NP	$T$ (K)	$a_N$ (G)	$a_{2H}$ (G)
-	300	16.25	10.14
-	340	16.22	9.80
NP1 <sup>a</sup>	300	15.20	8.50
NP1/6	300	15.23	8.55
NP1 <sup>a</sup>	340	15.35	8.46
NP1/6	340	15.32	8.44
NP2 <sup>a,b</sup>	300	<b>14.50</b>	<b>8.45</b>
	300	15.18	8.58
NP2/6 <sup>b</sup>	300	<b>14.59</b>	<b>8.50</b>
	300	15.10	8.65
NP2 <sup>a</sup>	340	15.15	8.50
NP2/6	340	15.13	8.60
NP3 <sup>a</sup>	300	15.15	8.40
NP3/6	300	15.10	8.50
NP3 <sup>a</sup>	340	15.40	8.48
NP3/6	340	15.33	8.40
NP4 <sup>a</sup>	300	<b>14.40<sup>b</sup></b>	<b>8.38<sup>b</sup></b>
	300	15.23	8.30
NP4/6	300	<b>14.30<sup>b</sup></b>	<b>8.50<sup>b</sup></b>
	300	15.35	8.35
NP4 <sup>a</sup>	340	15.32	8.40
NP4/6	340	15.28	8.36
NP5 <sup>a</sup>	300	15.25	8.35
NP5/6	300	15.30	8.55
NP5/6	340	15.22	8.50

<sup>a</sup>Data from ref 28. <sup>b</sup>The  $a_N$  values given in bold refer to the probe in the most hydrophobic location.

492 together with those previously<sup>28</sup> measured in the presence of  
 493 homoligand nanoparticles and in a temperature range between  
 494 300 and 340 K (for details on mixed-monolayer nanoparticle  
 495 synthesis, XPS characterization, and ESR measurements, see  
 496 the Experimental Section and SI Sections S2, S4, and S5;  
 497 otherwise, refer to our previous work<sup>28</sup>).

498 With NP1/6, NP3/6, and NP5/6 and their homoligand  
 499 partner, spectra are characterized by two different resolved sets  
 500 of signals (as an example, see Figure 9) at 300 K. The one with  
 501 larger hyperfine coupling constants is due to the probe located  
 502 in water, while the second one, has nitrogen hfsc's ( $a_N$ ,  
 503 reported in Table 1) significantly smaller than that measured  
 504 for 7 in solution, resulting from the probe positioned in the  
 505 monolayer. Analysis of the spectra suggests the presence of a  
 506 single interaction site, in line with the SOAP-GMM analysis for  
 507 nanoparticles having short chain shells.

508 In all thick monolayers (namely, NP2- and NP4-type  
 509 systems), the ESR analysis shows the presence of two distinct  
 510 environments, where the probe bound to the monolayer

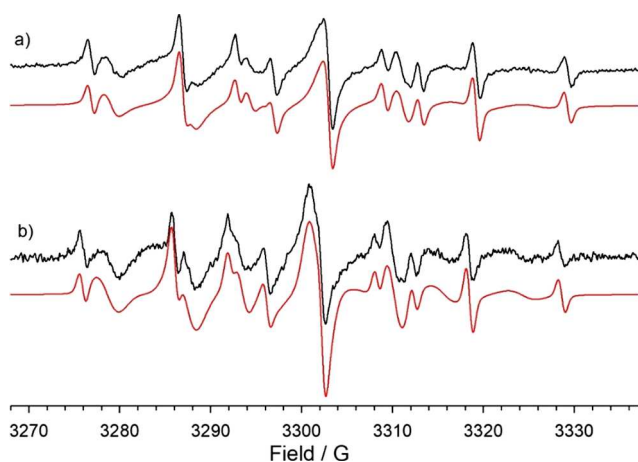


**Figure 9.** ESR spectra of the radical probe 7 recorded in water in the presence of NP3/6 (a) and NP4/6 (b) at 300 K. In red are reported the corresponding theoretical simulations obtained by employing the spectroscopic parameters reported in Table 1.

511 experiences different background polarities (Table 1). The first  
512 one has experimental values of  $a_N$  in the range of 14.30–14.60  
513 G, significantly smaller than that for the probe in water (16.26  
514 G), indicating an extremely low polarity. This is consistent  
515 with type-2 settings, where 7 lies close to the gold core and the  
516 overall hydration is limited, thus corresponding to NP2<sub>2</sub>,  
517 NP4<sub>1</sub>, NP2/6<sub>1</sub>, and NP4/6<sub>1</sub> states. In addition, such low  
518 values of  $a_N$  are seen only for long chain shells, in agreement  
519 with the SOAP-GMM classification (see Figure 8).

520 The second interaction location has much higher spectro-  
521 scopic parameters (15.10–15.35 G), closer to that of the probe  
522 free in solution, which are indeed associated with an increased  
523 environment polarity perceived by the probe. The existence of  
524 a second interaction site in NP2- and NP4-type systems  
525 parallels well the computational prediction, supporting the  
526 possibility to have distinguishable local environments within  
527 the same (thick) monolayer. Interestingly, the spectroscopic  
528 parameters are comparable to those for NP1-, NP3-, and NP5-  
529 type monolayers. This shows that the radical samples very  
530 similar environments in all these systems. SOAP similarity  
531 analysis returns a classification which is in line with this  
532 interpretation: in fact, NP2<sub>1</sub>, NP4<sub>2</sub>, NP2/6<sub>2</sub>, and NP4/6<sub>2</sub>  
533 environments are assigned to the same category (type-1  
534 class) as NP1(/6), NP3(/6), and NP5(/6) environments  
535 (Figure 8).

536 By increasing the temperature, a new set of signals,  
537 characterized by spectroscopic parameters very similar to  
538 those previously measured in type-1 *loci* appears in the  
539 spectrum, as was also seen by repeating the SOAP-GMM  
540 analysis including the most stable states at 340 K (Figures S10  
541 and S11). Hence, when the temperature is increased, the probe  
542 experiences local environments with higher polarity, solvation,  
543 and exposure to the surroundings that makes type-1 sites the  
544 most favorable interaction locations for the systems under  
545 investigation.

546 Quite unexpectedly, based on our current understand-  
547 ing,<sup>26,57</sup> the spectroscopic parameters of the probe in mixed-  
548 monolayer NPs do not differ significantly from those measured  
549 in the corresponding homoligand shell. Previous evidence on  
550 the monolayers made by mixtures of hydrocarbon/perfluor-  
551 ocarbon chains terminating with a short poly(oxoethylene)  
552 moiety indeed suggested that the probe should preferentially

reside in fluorinated domains. Here, instead, MD calculations 553  
clearly show that 7 never enters or fully interacts with the 554  
fluorinated patches and is located preferably at the fluorine 555  
domain interface (and thus explains the similarity in the 556  
nitrogen hspcs). In addition, MD calculations and Voronoi 557  
diagrams display that short F-alkyl chains are densely packed in 558  
the NPs considered here, physically and energetically 559  
preventing them to host the radical probe. 560

## CONCLUSIONS 561

In summary, ligands self-assembling on the surface of gold 562  
nanoparticles can create local (supra)molecular environments 563  
with unique fingerprints that allow them to be precisely 564  
detected and exploited. We have presented a computational 565  
approach, which enables automated identification and 566  
comparison of such environments driven from the data (i.e., 567  
from atomistic MD trajectories) and without feeding input 568  
parameters. The computational workflow is built on 569  
unsupervised clustering of the Smooth Overlap of Atomic 570  
Position (SOAP) atomic descriptors and a simple SOAP 571  
metric to classify the environments. In this proof-of-concept 572  
study, we have considered a collection of chemically different 573  
SAM-AuNPs, bearing cationic, anionic, and zwitterionic 574  
surface groups and having different monolayer thicknesses. 575  
The set includes homo- and heteroligand monolayers; the 576  
second ones present alternating hydrophilic/hydrophobic 577  
surface patterns that stem from the nanoscale separation of 578  
two immiscible ligands. By the SOAP analysis and in 579  
conjunction with ESR measures, we have successfully 580  
demonstrated that multiple structural and chemical micro- 581  
environments can exist together within the SAM-AuNPs 582  
investigated. In particular, they differ for accessibility, local 583  
solvation, and hydrophobicity, which are imparted by specific 584  
ligand length, nature of the ligand end group, and monolayer 585  
3D structure. 586

The results of our investigation allow us to draw some 587  
general conclusions: (i) anisotropic monolayers may facilitate 588  
the establishment of settings having well-defined and easily 589  
distinguishable local (supra)molecular motifs; (ii) in the 590  
absence of chemical groups designed to recreate specifically 591  
intended binding or catalytic sites, thick monolayers naturally 592  
lead to multiple, coexisting environments, which are shaped by 593  
confined solvent, organization, and conformational mobility of 594  
the ligands; (iii) surface patterns in heteroligand shells give rise 595  
to a multiplicity of states, which could be potentially targeted 596  
under appropriate thermodynamic or kinetic pathways. 597

Overall, this work provides a promising general approach for 598  
systematic and computationally efficient investigation of local 599  
(supra)molecular environments in SAM-AuNPs, a widely used 600  
class of O–I nanomaterials, and establishes a mechanistic 601  
understanding of their intimate features with a full account of 602  
nanoscale effects. The next steps will be the extension to more 603  
complex functional nanoparticles and the design guided by 604  
machine-learning algorithms of local motifs with predefined 605  
properties. 606

## EXPERIMENTAL SECTION 607

**Nanoparticle Synthesis and Characterization.** Detailed 608  
synthetic procedures and characterization for mixed monolayers 609  
nanoparticles can be found in the Supporting Information; otherwise, 610  
the reader may refer to our previous work.<sup>28</sup> All commercial reagents 611  
were purchased from Aldrich and VWR and used without purification 612  
unless otherwise mentioned. Solvents were purchased from Aldrich 613



614 and VWR and deuterated solvents, from Cambridge Isotope  
615 Laboratories and Aldrich. Dry solvents were obtained from Aldrich.  
616 Chlorinated solvents were kept over  $K_2CO_3$  for at least 24 h prior to  
617 use. All other solvents were reagent grade and used as received.  
618 Reactions were monitored by TLC on Merck silica gel plates (0.25  
619 mm) and visualized by UV light,  $I_2$ , or  $KMnO_4-H_2SO_4$  solution.  
620 Chromatography was performed on Merck silica gel 60F-254 (230–  
621 400 mesh), and the solvents employed were of analytical grade. NMR  
622 spectra were recorded on a Varian 500 spectrometer (operating at 500  
623 MHz for proton and at 125 MHz for  $^{13}C$ ) or on a Varian 400 MHz  
624 (operating at 400 for proton, at 376.16 MHz for  $^{19}F$ , and at 100.5  
625 MHz for carbon).  $^1H$  NMR chemical shifts were referenced to the  
626 residual protons in the deuterated solvent.  $^{19}F$  NMR spectra were  
627 referenced to  $CFCl_3$  chemical shift, and  $^{13}C$  NMR chemical shifts  
628 were referenced to the solvent chemical shift. Chemical shifts ( $\delta$ ) are  
629 reported in ppm, and the multiplicity of each signal is designated by  
630 the conventional abbreviations: s, singlet; d, doublet; t, triplet; q,  
631 quartet; m, multiplet; br, broad; dd, doublet of doublets. Coupling  
632 constants ( $J$ ) are quoted in Hz. UV–visible spectra were recorded on  
633 a Shimadzu UV-1800 spectrophotometer. TGA analyses were  
634 performed on TGA Q500 V6.3 Build 189 using a heating rate of  
635  $10\text{ }^\circ\text{C min}^{-1}$  up to  $1000\text{ }^\circ\text{C}$  under  $N_2$  flow. TEM images were  
636 obtained with a Jeol 3010 high resolution electron microscope (1.7  
637 nm point-to-point) operating at 300 keV using a Gatan slow-scan  
638 CCD camera (mod. 794). TEM samples of protected gold  
639 nanoparticles were prepared by placing a single drop of  $0.5\text{ mg mL}^{-1}$   
640 MeOH or  $H_2O/iPrOH$  solution onto a 200-mesh copper grid  
641 coated with an amorphous carbon film. NP gold core diameters were  
642 measured manually using a Gatan software Digital Micrograph on at  
643 least 200 particles. Electrospray ionization (ESI) mass analyses were  
644 performed on a PerkinElmer APII at 5600 eV and exact mass analyses,  
645 on a Bruker Daltonics microTOF-Q operating at 3200 V capillary  
646 potential. DLS measurements have been performed on a Malvern zeta  
647 Sizer Nano using a concentration for the nanoparticles between 0.1  
648 and  $0.4\text{ mg/mL}$  in water, scattering angle of  $173^\circ$ ,  $25\text{ }^\circ\text{C}$ , and  
649 disposable cuvettes.

650 **Molecular Modeling Methods.** A coarse-grained (CG) simu-  
651 lation approach based on dissipative particle dynamics (DPD) was  
652 first adopted to retrieve the phase separation of ligands on a gold  
653 surface in mixed SAMs, namely, nanoparticles NP1–5/6. This choice  
654 was necessary since the self-organization of chains requires long times  
655 that cannot be accessed simply by atomistic calculations. Once  
656 obtained, the CG nanoparticle model was mapped back onto the  
657 corresponding all-atom (AA) nanoparticle structure. Homoligand  
658 SAMs were modeled purely at atomic level. The full computational  
659 procedure for constructing the CG and AA SAM-functionalized NPs  
660 follows our previous works<sup>21,22,27,29,38</sup> and is described in detail in the  
661 **Supporting Information**. AA nanoparticle models in explicit water  
662 were then extracted from equilibrated MD trajectories and used for  
663 subsequent MD and SOAP-GMM analysis. CG calculations were  
664 carried out in a Culgi simulation package (v.12.0, Culgi B.V., Leiden,  
665 The Netherlands) and AA simulations, in an AMBER 18 modeling  
666 suite.

667 **MD and SOAP-GMM Analysis.** MD analysis was generated with  
668 a combination of an AMBER analysis tool, in-house developed  
669 Python codes, and Python package *scipy*.<sup>58</sup> SOAP descriptors were  
670 derived by using the *Describe*<sup>59</sup> Python package. For GMM  
671 clusterization and environment classification, we adopted the *scikit-*  
672 *learn*<sup>60</sup> Python package. The parameter setting is given in the  
673 **Supporting Information**.

674 **Electron Spin Resonance (ESR) Measurements.** ESR spectra  
675 were collected using a Bruker ELEXYS spectrometer equipped with  
676 an NMR gaussmeter for field calibration. The sample temperature was  
677 controlled with a standard variable temperature accessory and  
678 monitored before and after each run using a copper-constantan  
679 thermocouple. The instrument settings were as follows: microwave  
680 power 5.0 mW, modulation amplitude 0.05 mT, modulation  
681 frequency 100 kHz, and scan time 180 s. Digitized EPR spectra  
682 were transferred to a personal computer for analysis using digital

simulations carried out with a program developed in our laboratory  
683 and based on a Monte Carlo procedure. 684

**Synchrotron-Based X-ray Photoelectron Spectroscopy**  
(XPS) Measurements. Synchrotron-based X-ray photoelectron  
685 spectroscopy (XPS) experiments were carried out at the Material  
686 Science beamline of the Elettra synchrotron radiation facility in  
687 Trieste, Italy. The NPs were dispersed in aqueous solution and then  
688 drop-casted on a *n*-doped Si wafer, capped with a layer of native oxide  
689 (thickness of the oxide  $\sim 4\text{ nm}$ ). After drying the samples for 24 h in a  
690 protected environment at atmospheric pressure, they were inserted in  
691 the experimental UHV chamber of the beamline and promptly  
692 measured. The base pressure during the experiment was ca.  $2 \times 10^{-10}$   
693 mbar. XPS spectra were acquired by means of a Specs Phoibos 150  
694 mm mean-radius electron energy analyzer, equipped with a 1D-delay  
695 line detector built in-house. The overall energy resolution of the  
696 experiment was ca. 200 meV. The photoelectrons were collected at a  
697 normal emission angle, and for each sample measured, the same  
698 acquisition conditions (pass energy, entrance slit, lens mode of the  
699 spectrometer) were used. The measured signal was normalized to the  
700 incoming photon current and to the number of sweeps. The  
701 decomposition of the core-level spectra was carried out by using  
702 Doniach–Sunjic profiles<sup>61</sup> convoluted with a Gaussian (to take into  
703 account the experimental resolution, the thermal effects, and the  
704 inhomogeneous broadening) on a linear background, thus obtaining  
705 the line shape parameters, the photoemission intensity (i.e., the area  
706 delimited by the peak), and the core electron binding energy (BE) for  
707 each spectral component. 708  
709

## ASSOCIATED CONTENT

### Supporting Information

The Supporting Information is available free of charge at  
712 <https://pubs.acs.org/doi/10.1021/acsnano.2c08467>. 713

Additional computational and experimental results,  
714 synthesis and characterization of mixed-monolayers  
715 nanoparticles, computational methods, ESR background,  
716 and details on XPS analysis (PDF) 717

## AUTHOR INFORMATION

### Corresponding Authors

- Paola Posocco – Department of Engineering and Architecture,  
720 University of Trieste, 34127 Trieste, Italy; [orcid.org/0000-0001-8129-1572](https://orcid.org/0000-0001-8129-1572); Email: [paola.posocco@dia.units.it](mailto:paola.posocco@dia.units.it) 721  
Lucia Pasquato – Department of Chemical and  
722 Pharmaceutical Sciences and INSTM Trieste Research Unit,  
723 University of Trieste, 34127 Trieste, Italy; [orcid.org/0000-0003-1842-9609](https://orcid.org/0000-0003-1842-9609); Email: [l.pasquato@units.it](mailto:l.pasquato@units.it) 724  
Marco Lucarini – Department of Chemistry “G. Ciamician”,  
725 University of Bologna, I-40126 Bologna, Italy; [orcid.org/0000-0002-8978-4707](https://orcid.org/0000-0002-8978-4707); Email: [marco.lucarini@unibo.it](mailto:marco.lucarini@unibo.it) 726  
727  
728  
729

### Authors

- Cristian Gabellini – Department of Engineering and  
730 Architecture, University of Trieste, 34127 Trieste, Italy 731  
Maria Sologan – Department of Chemical and  
732 Pharmaceutical Sciences and INSTM Trieste Research Unit,  
733 University of Trieste, 34127 Trieste, Italy 734  
Elena Pellizzoni – Department of Chemical and  
735 Pharmaceutical Sciences and INSTM Trieste Research Unit,  
736 University of Trieste, 34127 Trieste, Italy 737  
Domenico Marson – Department of Engineering and  
738 Architecture, University of Trieste, 34127 Trieste, Italy 739  
Mario Daka – Department of Chemical and Pharmaceutical  
740 Sciences and INSTM Trieste Research Unit, University of  
741 Trieste, 34127 Trieste, Italy 742  
743



744 **Paola Franchi** – Department of Chemistry “G. Ciamician”,  
745 University of Bologna, I-40126 Bologna, Italy  
746 **Luca Bignardi** – Department of Physics, University of Trieste,  
747 34127 Trieste, Italy; [orcid.org/0000-0002-9846-9100](https://orcid.org/0000-0002-9846-9100)  
748 **Stefano Franchi** – Elettra Sincrotrone Trieste, 34149 Trieste,  
749 Italy; [orcid.org/0000-0002-5009-9147](https://orcid.org/0000-0002-5009-9147)  
750 **Zbyšek Posel** – Department of Informatics, Jan Evangelista  
751 Purkyně University, 400 96 Ustí nad Labem, Czech  
752 Republic; [orcid.org/0000-0003-4271-5349](https://orcid.org/0000-0003-4271-5349)  
753 **Alessandro Baraldi** – Department of Physics, University of  
754 Trieste, 34127 Trieste, Italy  
755 **Paolo Pengo** – Department of Chemical and Pharmaceutical  
756 Sciences and INSTM Trieste Research Unit, University of  
757 Trieste, 34127 Trieste, Italy

758 Complete contact information is available at:  
759 <https://pubs.acs.org/10.1021/acsnano.2c08467>

## 760 Notes

761 The authors declare no competing financial interest.

## 762 ACKNOWLEDGMENTS

763 This work received support from the Italian Ministry of  
764 University Research through the projects “Structure and  
765 function at the nanoparticle biointerface” (RBSI14PBC6 to  
766 P. Posocco), PRIN2017 NiFTy (2017MYBTXC to L.P.),  
767 PRIN2017 “BacHounds: Supramolecular nanostructures for  
768 bacteria detection” (2017E44A9P to M.L.), and “Nemo”  
769 (20173L7W8K to P.F.). P. Pengo and C.G. are particularly  
770 grateful to the University of Trieste for scholarship support and  
771 acknowledge the CINECA award under the ISCRA initiative  
772 for the availability of high performance computing resources.  
773 CERIC-ERIC consortium is acknowledged for the access to  
774 the Material Science beamline at the Elettra synchrotron  
775 radiation facility (proposal number 20192081). The staff of the  
776 Material Science beamline is kindly acknowledged for technical  
777 support. Z.P. acknowledges the assistance provided by the  
778 Technology Agency of the Czech Republic, under the project  
779 Metamorph, project No. TO01000329.

## 780 REFERENCES

781 (1) Goodman, E. D.; Zhou, C.; Cargnello, M. Design of organic/  
782 inorganic hybrid catalysts for energy and environmental applications.  
783 *ACS Cent. Sci.* **2020**, *6*, 1916–1937.  
784 (2) Prins, L. J. Emergence of complex chemistry on an organic  
785 monolayer. *Acc. Chem. Res.* **2015**, *48*, 1920–1928.  
786 (3) Sun, X.; Riccardi, L.; De Biasi, F.; Rastrelli, F.; De Vivo, M.; et al.  
787 Molecular-dynamics-simulation-directed rational design of nano-  
788 receptors with targeted affinity. *Angew. Chem., Int. Ed.* **2019**, *58*,  
789 7702–7707.  
790 (4) Zeiri, O. Metallic-nanoparticle-based sensing: Utilization of  
791 mixed-ligand monolayers. *ACS Sens.* **2020**, *5*, 3806–3820.  
792 (5) Grommet, A. B.; Feller, M.; Klajn, R. Chemical reactivity under  
793 nanoconfinement. *Nat. Nanotechnol.* **2020**, *15*, 256–271.  
794 (6) Zhu, Q.; Murphy, C. J.; Baker, L. R. Opportunities for  
795 electrocatalytic CO<sub>2</sub> reduction enabled by surface ligands. *J. Am.*  
796 *Chem. Soc.* **2022**, *144*, 2829–2840.  
797 (7) Chu, Z.; Han, Y.; Bian, T.; De, S.; Král, P.; et al. Supramolecular  
798 control of azobenzene switching on nanoparticles. *J. Am. Chem. Soc.*  
799 **2019**, *141*, 1949–1960.  
800 (8) Szewczyk, M.; Sobczak, G.; Sashuk, V. Photoswitchable catalysis  
801 by a small swinging molecule confined on the surface of a colloidal  
802 particle. *ACS Catal.* **2018**, *8*, 2810–2814.

(9) Mati, I. K.; Edwards, W.; Marson, D.; Howe, E. J.; Stinson, S.;  
803 Kay, E. R.; et al. Probing multiscale factors affecting the reactivity of  
804 nanoparticle-bound molecules. *ACS Nano* **2021**, *15*, 8295–8305. 805  
(10) Kim, M.; Dygas, M.; Sobolev, Y. I.; Beker, W.; Zhuang, Q.;  
806 Grzybowski, B. A.; et al. On-nanoparticle gating units render an  
807 ordinary catalyst substrate- and site-selective. *J. Am. Chem. Soc.* **2021**,  
808 *143*, 1807–1815. 809  
(11) Cha, M.; Emre, E. S. T.; Xiao, X.; Kim, J.-Y.; Bogdan, P.; et al.  
810 Unifying structural descriptors for biological and bioinspired nano-  
811 scale complexes. *Nat. Comput. Sci.* **2022**, *2*, 243–252. 812  
(12) Siek, M.; Kandere-Grzybowska, K.; Grzybowski, B. A. Mixed-  
813 charge, pH-responsive nanoparticles for selective interactions with  
814 cells, organelles, and bacteria. *Acc. Mater. Res.* **2020**, *1*, 188–200. 815  
(13) Riccardi, L.; Gabrielli, L.; Sun, X.; De Biasi, F.; Rastrelli, F.;  
816 et al. Nanoparticle-based receptors mimic protein-ligand recognition.  
817 *Chem.* **2017**, *3*, 92–109. 818  
(14) Pecina, A.; Rosa-Gastaldo, D.; Riccardi, L.; Franco-Ulloa, S.;  
819 Milan, E.; et al. On the metal-aided catalytic mechanism for  
820 phosphodiester bond cleavage performed by nanozymes. *ACS Catal.*  
821 **2021**, *11*, 8736–8748. 822  
(15) Cao-Milán, R.; Gopalakrishnan, S.; He, L. D.; Huang, R.;  
823 Wang, L.-S.; et al. Thermally gated bio-orthogonal nanozymes with  
824 supramolecularly confined porphyrin catalysts for antimicrobial uses.  
825 *Chem.* **2020**, *6*, 1113–1124. 826  
(16) Zhang, X.; Huang, R.; Gopalakrishnan, S.; Cao-Milán, R.;  
827 Rotello, V. M. Bioorthogonal nanozymes: Progress towards  
828 therapeutic applications. *Trends Chem.* **2019**, *1*, 90–98. 829  
(17) Cao-Milán, R.; He, L. D.; Shorkey, S.; Tonga, G. Y.; Wang, L.-  
830 S.; et al. Modulating the catalytic activity of enzyme-like nanoparticles  
831 through their surface functionalization. *Mol. Syst. Des. Eng.* **2017**, *2*,  
832 624–628. 833  
(18) Huang, R.; Luther, D. C.; Zhang, X.; Gupta, A.; Tufts, S. A.;  
834 et al. Engineering the interface between inorganic nanoparticles and  
835 biological systems through ligand design. *Nanomaterials* **2021**, *11*,  
836 1001. 837  
(19) Wu, M.; Vartanian, A. M.; Chong, G.; Pandiakumar, A. K.;  
838 Hamers, R. J.; et al. Solution NMR analysis of ligand environment in  
839 quaternary ammonium-terminated self-assembled monolayers on gold  
840 nanoparticles: The effect of surface curvature and ligand structure. *J.*  
841 *Am. Chem. Soc.* **2019**, *141*, 4316–4327. 842  
(20) Liu, X.; Yu, M.; Kim, H.; Mameli, M.; Stellacci, F.  
843 Determination of monolayer-protected gold nanoparticle ligand-  
844 shell morphology using NMR. *Nat. Commun.* **2012**, *3*, 1182. 845  
(21) Şologan, M.; Marson, D.; Polizzi, S.; Pengo, P.; Boccardo, S.;  
846 et al. Patchy and Janus nanoparticles by self-organization of mixtures  
847 of fluorinated and hydrogenated alkanethiolates on the surface of a  
848 gold core. *ACS Nano* **2016**, *10*, 9316–9325. 849  
(22) Luo, Z.; Marson, D.; Ong, Q. K.; Loiudice, A.; Kohlbrecher, J.;  
850 et al. Quantitative 3D determination of self-assembled structures on  
851 nanoparticles using small angle neutron scattering. *Nat. Commun.*  
852 **2018**, *9*, 1343. 853  
(23) Luo, Z.; Zhao, Y.; Darwish, T.; Wang, Y.; Hou, J.; et al. Mass  
854 spectrometry and Monte Carlo method mapping of nanoparticle  
855 ligand shell morphology. *Nat. Commun.* **2018**, *9*, 4478. 856  
(24) Lucarini, M.; Franchi, P.; Pedulli, G. F.; Pengo, P.; Scrimin, P.;  
857 et al. EPR study of dialkyl nitroxides as probes to investigate the  
858 exchange of solutes between the ligand shell of monolayers of  
859 protected gold nanoparticles and aqueous solutions. *J. Am. Chem. Soc.*  
860 **2004**, *126*, 9326–9329. 861  
(25) Lucarini, M.; Pasquato, L. ESR spectroscopy as a tool to  
862 investigate the properties of self-assembled monolayers protecting  
863 gold nanoparticles. *Nanoscale* **2010**, *2*, 668–676. 864  
(26) Posocco, P.; Gentilini, C.; Bidoggia, S.; Pace, A.; Franchi, P.;  
865 et al. Self-organization of mixtures of fluorocarbon and hydrocarbon  
866 amphiphilic thiolates on the surface of gold nanoparticles. *ACS Nano*  
867 **2012**, *6*, 7243–7253. 868  
(27) Marson, D.; Posel, Z.; Posocco, P. Molecular features for  
869 probing small amphiphilic molecules with self-assembled monolayer-  
870 protected nanoparticles. *Langmuir* **2020**, *36*, 5671–5679. 871

- 872 (28) Pellizzoni, E.; Şologan, M.; Daka, M.; Pengo, P.; Marson, D.;  
873 et al. Thiolate end-group regulates ligand arrangement, hydration and  
874 affinity for small compounds in monolayer-protected gold nano-  
875 particles. *J. Colloid Interface Sci.* **2022**, *607*, 1373–1381.
- 876 (29) Marson, D.; Guida, F.; Şologan, M.; Boccardo, S.; Pengo, P.;  
877 et al. Mixed fluorinated/hydrogenated self-assembled monolayer-  
878 protected gold nanoparticles: *In silico* and *in vitro* behavior. *Small*  
879 **2019**, *15*, 1900323.
- 880 (30) Musil, F.; Grisafi, A.; Bartók, A. P.; Ortner, C.; Csányi, G.; et al.  
881 Physics-inspired structural representations for molecules and materi-  
882 als. *Chem. Rev.* **2021**, *121*, 9759–9815.
- 883 (31) Gasparotto, P.; Meißner, R. H.; Ceriotti, M. Recognizing local  
884 and global structural motifs at the atomic scale. *J. Chem. Theory* **2018**,  
885 *14*, 486–498.
- 886 (32) Shyshov, O.; Haridas, S. V.; Pesce, L.; Qi, H.; Gardin, A.; et al.  
887 Living supramolecular polymerization of fluorinated cyclohexanes.  
888 *Nat. Commun.* **2021**, *12*, 3134.
- 889 (33) Ofir, Y.; Samanta, B.; Arumugam, P.; Rotello, V. M. Controlled  
890 fluorination of FePt nanoparticles: Hydrophobic to superhydrophobic  
891 surfaces. *Adv. Mater.* **2007**, *19*, 4075–4079.
- 892 (34) Marsh, Z. M.; Lantz, K. A.; Stefik, M. QCM detection of  
893 molecule–nanoparticle interactions for ligand shells of varying  
894 morphology. *Nanoscale* **2018**, *10*, 19107–19116.
- 895 (35) Elbert, K. C.; Jishkariani, D.; Wu, Y.; Lee, J. D.; Donnio, B.;  
896 et al. Design, self-assembly, and switchable wettability in hydrophobic,  
897 hydrophilic, and Janus dendritic ligand–gold nanoparticle hybrid  
898 materials. *Chem. Mater.* **2017**, *29*, 8737–8746.
- 899 (36) Basham, C. M.; Premadasa, U. I.; Ma, Y.-Z.; Stellacci, F.;  
900 Doughty, B.; et al. Nanoparticle-induced disorder at complex liquid–  
901 liquid interfaces: Effects of curvature and compositional synergy on  
902 functional surfaces. *ACS Nano* **2021**, *15*, 14285–14294.
- 903 (37) Pan, S.; Richardson, J. J.; Christofferson, A. J.; Besford, Q. A.;  
904 Zheng, T.; et al. Fluorinated metal–organic coatings with selective  
905 wettability. *J. Am. Chem. Soc.* **2021**, *143*, 9972–9981.
- 906 (38) Edwards, W.; Marro, N.; Turner, G.; Kay, E. R. Continuum  
907 tuning of nanoparticle interfacial properties by dynamic covalent  
908 exchange. *Chem. Sci.* **2018**, *9*, 125–133.
- 909 (39) Stewart, A.; Zheng, S.; McCourt, M. R.; Bell, S. E. J.  
910 Controlling assembly of mixed thiol monolayers on silver nano-  
911 particles to tune their surface properties. *ACS Nano* **2012**, *6*, 3718–  
912 3726.
- 913 (40) Pengo, P.; Şologan, M.; Pasquato, L.; Guida, F.; Pacor, S.; et al.  
914 Gold nanoparticles with patterned surface monolayers for nano-  
915 medicine: Current perspectives. *Eur. Biophys. J.* **2017**, *46*, 749–771.
- 916 (41) Luo, Z.; Hou, J.; Menin, L.; Ong, Q. K.; Stellacci, F. Evolution  
917 of the ligand shell morphology during ligand exchange reactions on  
918 gold nanoparticles. *Angew. Chem., Int. Ed.* **2017**, *56*, 13521–13525.
- 919 (42) Singh, C.; Ghorai, P. K.; Horsch, M. A.; Jackson, A. M.; Larson,  
920 R. G.; et al. Entropy-mediated patterning of surfactant-coated  
921 nanoparticles and surfaces. *Phys. Rev. Lett.* **2007**, *99*, 226106.
- 922 (43) Bock, M.; Tyagi, A. K.; Kreft, J.-U.; Alt, W. Generalized  
923 Voronoi tessellation as a model of two-dimensional cell tissue  
924 dynamics. *Bull. Math. Biol.* **2010**, *72*, 1696–1731.
- 925 (44) Liang, D.; Dahal, U.; Wu, M.; Murphy, C. J.; Cui, Q. Ligand  
926 length and surface curvature modulate nanoparticle surface hetero-  
927 geneity and electrostatics. *J. Phys. Chem. C* **2020**, *124*, 24513–24525.
- 928 (45) Kelkar, A. S.; Dallin, B. C.; Lehn, R. C. V. Identifying  
929 nonadditive contributions to the hydrophobicity of chemically  
930 heterogeneous surfaces via dual-loop active learning. *J. Chem. Phys.*  
931 **2022**, *156*, 024701.
- 932 (46) Chew, A. K.; Dallin, B. C.; Van Lehn, R. C. The interplay of  
933 ligand properties and core size dictates the hydrophobicity of  
934 monolayer-protected gold nanoparticles. *ACS Nano* **2021**, *15*,  
935 4534–4545.
- 936 (47) Hoff, S. E.; Di Silvio, D.; Ziolo, R. F.; Moya, S. E.; Heinz, H.  
937 Patterning of self-assembled monolayers of amphiphilic multisegment  
938 ligands on nanoparticles and design parameters for protein  
939 interactions. *ACS Nano* **2022**, *16*, 8766–8783.
- (48) Luo, Z.; Murello, A.; Wilkins, D. M.; Kovacik, F.; Kohlbrecher, 940  
J.; et al. Determination and evaluation of the nonadditivity in wetting 941  
of molecularly heterogeneous surfaces. *Proc. Natl. Acad. Sci. U. S. A.* 942  
**2019**, *116*, 25516–25523. 943
- (49) Bartók, A. P.; Kondor, R.; Csányi, G. On representing chemical 944  
environments. *Phys. Rev. B* **2013**, *87*, 184115. 945
- (50) Musil, F.; De, S.; Yang, J.; Campbell, J. E.; Day, G. M.; et al. 946  
Machine learning for the structure–energy–property landscapes of 947  
molecular crystals. *Chem. Sci.* **2018**, *9*, 1289–1300. 948
- (51) Bartók, A. P.; De, S.; Poelking, C.; Bernstein, N.; Kermode, J. 949  
R.; et al. Machine learning unifies the modeling of materials and 950  
molecules. *Sci. Adv.* **2017**, *3*, e1701816. 951
- (52) de Marco, A. L.; Boichichio, D.; Gardin, A.; Doni, G.; Pavan, 952  
G. M. Controlling exchange pathways in dynamic supramolecular 953  
polymers by controlling defects. *ACS Nano* **2021**, *15*, 14229–14241. 954
- (53) De, S.; Bartók, A. P.; Csányi, G.; Ceriotti, M. Comparing 955  
molecules and solids across structural and alchemical space. *Phys.* 956  
*Chem. Chem. Phys.* **2016**, *18*, 13754–13769. 957
- (54) Ionita, P.; Carageorghopol, A.; Gilbert, B. C.; Chechik, V. 958  
EPR study of a place-exchange reaction on Au nanoparticles: Two 959  
branches of a disulfide molecule do not adsorb adjacent to each other. 960  
*J. Am. Chem. Soc.* **2002**, *124*, 9048–9049. 961
- (55) Lucarini, M.; Franchi, P.; Pedulli, G. F.; Gentilini, C.; Polizzi, 962  
S.; et al. Effect of core size on the partition of organic solutes in the 963  
monolayer of water-soluble nanoparticles: An ESR investigation. *J.* 964  
*Am. Chem. Soc.* **2005**, *127*, 16384–16385. 965
- (56) Gentilini, C.; Evangelista, F.; Rudolf, P.; Franchi, P.; Lucarini, 966  
M.; et al. Water-soluble gold nanoparticles protected by fluorinated 967  
amphiphilic thiolates. *J. Am. Chem. Soc.* **2008**, *130*, 15678–15682. 968
- (57) Gentilini, C.; Franchi, P.; Mileo, E.; Polizzi, S.; Lucarini, M.; 969  
et al. Formation of patches on 3D sams driven by thiols with 970  
immiscible chains observed by ESR spectroscopy. *Angew. Chem., Int.* 971  
*Ed.* **2009**, *48*, 3060–3064. 972
- (58) Virtanen, P.; Gommers, R.; Oliphant, T. E.; Haberland, M.; 973  
Reddy, T.; et al. Scipy 1.0: Fundamental algorithms for scientific 974  
computing in Python. *Nat. Methods* **2020**, *17*, 261–272. 975
- (59) Himanen, L.; Jäger, M. O. J.; Morooka, E. V.; Federici Canova, 976  
F.; Ranawat, Y. S.; et al. Dscribe: Library of descriptors for machine 977  
learning in materials science. *Comput. Phys. Commun.* **2020**, *247*, 978  
106949. 979
- (60) Pedregosa, F.; Varoquaux, G.; Gramfort, A.; Michel, V.; 980  
Thirion, B.; et al. Scikit-learn: Machine learning in Python. *J. Mach.* 981  
*Learn. Res.* **2011**, *12*, 2825–2830. 982
- (61) Doniach, S.; Sunjic, M. Many-electron singularity in X-ray 983  
photoemission and X-ray line spectra from metals. *J. Phys. C Solid* 984  
*State Phys.* **1970**, *3*, 285–291. 985